

Through-pellicle imaging of extreme ultraviolet mask with extreme ultraviolet ptychography microscope

Dong Gon Woo
Young Woong Kim
Yong Ju Jang
Seong Ju Wi
Jinho Ahn

Through-pellicle imaging of extreme ultraviolet mask with extreme ultraviolet ptychography microscope

Dong Gon Woo,^a Young Woong Kim,^a Yong Ju Jang,^b Seong Ju Wi,^a and Jinho Ahn^{a,c,*}

^aHanyang University, Department of Materials Science and Engineering, Seoul, Republic of Korea

^bHanyang University, Department of Nanoscale Semiconductor Engineering, Seoul, Republic of Korea

^cHanyang University, Institute of Nano Science and Technology, Seoul, Republic of Korea

Abstract

Background: An extreme ultraviolet (EUV) pellicle is necessary to increase the process yield even though the declining throughput is a big concern. However, an EUV metrology/inspection tool for this pellicle has not been commercialized yet.

Aim: The goal of this study is to verify the pellicle/mask inspection feasibility of EUV scanning lensless imaging (ESLI) and verify the impact of contaminants on pellicles depending on their size.

Approach: Through-pellicle imaging was implemented by using ESLI, which uses a high-order harmonic generation EUV source and ptychography. Optical characteristics of various sizes of Fe-contaminated EUV pellicles were evaluated to verify their impact on wafer images.

Results: Large size ($\sim 10 \mu\text{m}$) contaminants on the pellicle were found to contribute to the final wafer pattern loss. However, small size (2 to 3 μm) contaminants on the pellicle do not have substantial impact on the wafer image.

Conclusions: The defect detection capability of ESLI for pellicle and mask was confirmed. Therefore, ESLI is useful in applications like pellicle qualification and EUV mask inspection metrology.

© The Authors. Published by SPIE under a Creative Commons Attribution 4.0 Unported License. Distribution or reproduction of this work in whole or in part requires full attribution of the original publication, including its DOI. [DOI: [10.1117/1.JMM.18.3.034005](https://doi.org/10.1117/1.JMM.18.3.034005)]

Keywords: extreme ultraviolet lithography; extreme ultraviolet pellicle; extreme ultraviolet mask; ptychography.

Paper 19060 received Jul. 8, 2019; accepted for publication Aug. 29, 2019; published online Sep. 28, 2019.

1 Introduction

Extreme ultraviolet lithography (EUVL), which has been developed for more than 30 years, is expected to be employed in high-volume manufacturing (HVM) of 7-nm technology-node devices in 2019.^{1,2} The availability of pellicles, which protect a mask from particles generated during the lithography process, has long been an issue. The opinion that the EUV pellicle is necessary to increase the process yield is dominant even though declining throughput is a big concern. Also, EUV metrology/inspection technologies have been developed for a long time, but there is no commercialized tool for HVM available yet. Metrology/inspection techniques that use deep ultraviolet or E-beam light sources can be applied for preliminary investigation of EUV masks, but actinic techniques using 13.5-nm wavelength are known to be necessary for precise measurement of aerial critical dimensions (CDs) and unflawing detection of printable defects.^{3–12}

In this study, EUV scanning lensless imaging (ESLI), which uses a coherent EUV light source generated by high-harmonic generation (HHG) and coherent diffractive imaging (CDI), is introduced, which can be applied for inspection/metrology of EUV masks with or without pellicles. We have already reported quantitative analysis of the phase shift effect of EUV phase shift mask using single-shot CDI engines, such as error reduction algorithm (ERA) and

hybrid input–output (HIO) algorithm.^{13–17} However, in the case of single-shot CDI, the field-of-view is limited by the size of the inspection beam at the mask plane (3 μm diameter). Also, the information of light source and object cannot be deconvolved, and this makes an accurate analysis of the object difficult. In order to overcome these limitations of single-shot CDI, ptychography is introduced, which reconstructs the object image by using sequential diffraction patterns with redundancy. We verified the feasibility of ESLI, which uses multishot CDI with HHG source, as an actinic inspection/metrology technique for EUV masks even with pellicles. For the purpose of evaluation, an EUV mask with 128-nm 1:1 half-pitch (HP) line and space (L/S) patterns was imaged and the results were compared with those obtained using a commercialized critical dimension-scanning electron microscope (CD-SEM) tool. Also, the optical impact of particle contamination on EUV pellicle was analyzed to verify its potential printability during the lithography process.

2 Experimental Setup

2.1 System Overview

As shown in Fig. 1, the ESLI system consists of a source chamber, where EUV light is generated, and an optic chamber, where the object is illuminated and diffracted lights are captured. The EUV light for actinic inspection is generated by HHG. A 800-nm wavelength Ti:sapphire laser with 50-fs duration is used as the driving laser. The pulse energy and

*Address all correspondence to Jinho Ahn, E-mail: jhahn@hanyang.ac.kr

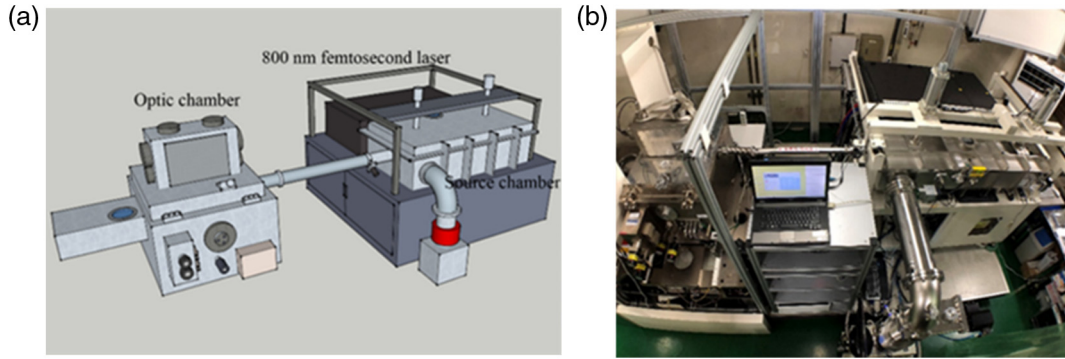


Fig. 1 (a) Schematic and (b) real image of EUV ESLI system. The footprint of ESLI system is about $1.8 \times 3.5 \times 1.5 \text{ m}^3$ (WDH).

repetition rate of the driving laser are 4.0 mJ and 1 kHz, respectively. Intense and coherent harmonics are emitted by focusing femtosecond laser pulses into noble gases, such as Ne. Since the HHG process is temporally symmetric, only odd-order harmonics are emitted.¹⁸ ESLI filters out other harmonics and only uses the 59th harmonic, which is equivalent to a wavelength of 13.55 nm. The photon flux of the EUV light is about $2.3 \times 10^8 \text{ photons s}^{-1} \text{ m}^{-2}$.

Since strict and stable probe information is an urgent requirement in ptychographic imaging, stability of the EUV source is essential.¹⁹ The intensity of the emitted harmonic pulse is strongly related to the number of atoms in the interaction region, where the noble gas and driving laser interact.¹⁸ In order to obtain stable EUV light with steady intensity, a stabilizer system that uses a closed-loop feedback system, which monitors the output (EUV intensity) and controls the input (driving laser path), was applied.

The EUV scanner is designed to have 6-deg incident angle with reflective optics. Therefore, the optic system of ESLI was also designed to irradiate EUV light onto a mask with 6-deg incident angle with a EUV spherical mirror and a plane mirror, as shown in Fig. 2. The focal length of the spherical mirror is 165 mm, and the objective lens is omitted as the lensless imaging says. As shown in Fig. 2, EUV light diffracted from the sample is captured in far-field diffraction condition with a charge-coupled device (CCD) detector (PI-MTE 2048B CCD with 2048 \times 2048 pixels) The distance between the sample and detector is 109 mm and the

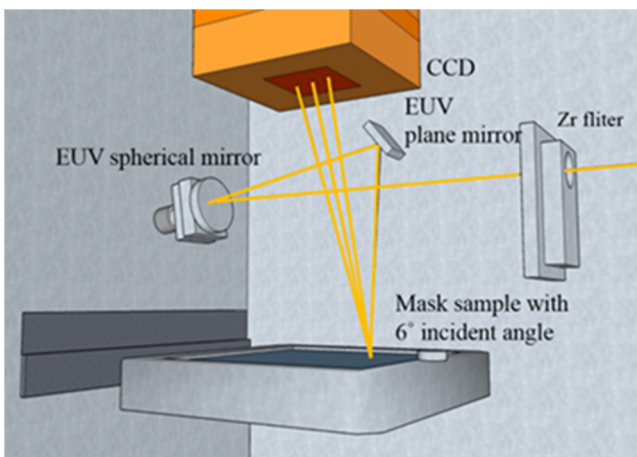


Fig. 2 Optic system of ESLI.

detecting area of the CCD is $27.6 \times 27.6 \text{ mm}^2$. The overlap distance between each probing area (at least $\sim 10\%$ required) should be accurate in order to obtain clear image by using ptychography.¹⁹ Inaccuracy in the stepping distance of the sample stage deteriorates the resolution of the final reconstructed image. The resolution of 6" EUV mask loadable stage is about 200 nm and the position accuracy is about 100 nm (AIREX corporation linear motor P16 and P20). Each dataset was captured with data correction, which subtracts the background detector noise. In order to minimize inherent noise, the CCD was operated at -50°C . Electromagnetic noise from the stage can be another noise source for reconstruction. Therefore, electromagnetic shielding such as Mu-metal shielding was applied to the system.

2.2 Image Reconstruction Method

Reconstruction of the object image is obtained using CDI. Several approaches, such as ERA, HIO algorithm, and ptychography, are commonly used to retrieve the missing phase information and to provide complex information about the object. Among them, ptychography is one of the emerging techniques in CDI. Various kinds of ptychography, such as difference map, conjugate gradient, and ptychographical iterative engine (PIE), are suggested to solve the phase problem of multiple diffraction patterns. Since PIE shows reasonable convergence rate and robustness in finding the solution, we used a PIE-based algorithm for image reconstruction.¹⁹ Also, we applied extended PIE (ePIE) and position correcting PIE (pcPIE)²⁰⁻²³ to compensate the physical errors caused by position inaccuracy of the stage and thermal drift.

The initial guess of exit wave of j 'th captured position is formed by multiplying the object guess by probe guess. Since a coherent system is linear in complex amplitude, the exit wave can be expressed as in Eq. (1):

$$\psi_{jr} = O_j(r)P_j(r). \quad (1)$$

Therefore, measured diffraction intensities, I_{ju} , which are captured in far-field diffraction condition, are defined as in Eq. (2):

$$I_{ju} = \mathcal{F}[O_j(r)P_j(r)], \quad (2)$$

where r and u represent real space and reciprocal space coordinates, respectively, and $P_j(r)$ and $O_j(r)$ indicate probe and object wavefronts.

The obtained diffraction patterns provide information in reciprocal space. Therefore, the exit wave propagating to the detector plane and should be backpropagated into real space, via Fourier constraint, replacing the amplitude with the square of the measured diffraction intensity. The initial guess of ψ_{jr} is the multiplication of random probe and random object. Propagation of guessed exit wave to the detector plane is performed by discrete Fourier transform. Then, the modulus of the measured intensity is replaced, which is called modulus or Fourier constraint. Discrete inverse Fourier transform was performed in order to calculate back-propagation of the diffracted signal to the real space, providing the revised exit wave ψ'_{jr} .²⁴ Revised exit wave can be expressed as in Eq. (3):

$$\psi'_{jr} = \mathcal{F}^{-1} \left[\sqrt{I_{jr}} \frac{\mathcal{F}[\psi_{jr}]}{|\mathcal{F}[\psi_{jr}]|} \right]. \quad (3)$$

Revised exit waves are updated according to the ePIE update equation expressed below:²⁰

$$O_{j+1}(r) = O_j(r) + \alpha \frac{P_j^*(r - R_{s(j)})}{|P_j(r - R_{s(j)})|_{\max}^2} (\psi'_{jr} - \psi_{jr}), \quad (4)$$

$$P_{j+1}(r) = P_j(r) + \beta \frac{O_j^*(r + R_{s(j)})}{|O_j(r + R_{s(j)})|_{\max}^2} (\psi'_{jr} - \psi_{jr}). \quad (5)$$

The step size, $R_{s(j)}$, was decided to guarantee sufficient redundancy between the diffraction patterns, considering the probe with a diameter of about $3 \mu\text{m}$. The reconstructed images were obtained by hundreds of iterations of ePIE and pcPIE. Schematic process of ptychography is displayed in

Fig. 3. We concluded the iteration number when sum squared errors were smaller than 10^{-6} . Sum squared errors were calculated at every pixel of the reconstructed image. The number of iterations was determined by the convergence of the algorithm.

3 Results and Discussion

Figure 4 shows the comparison of mask images of 128-nm HPL/S patterns, which were Fig. 4(a) measured by CD-SEM and Fig. 4(b) reconstructed by ESLI. Figure 4(b) is a cropped image of ESLI, which was reconstructed with 5×5 diffraction patterns with a step size of $1 \mu\text{m}$ between the scan positions, resulting in about $10 \times 10 \mu\text{m}^2$. The size of the cropped ESLI image was about $6 \times 6 \mu\text{m}^2$. Since the detector to sample distance is 109 mm and the detector size is 27.6 mm^2 (PI-MTE 2048B), the theoretical numerical aperture (NA) of ESLI is 0.1256. Therefore, the pixel size of the reconstructed image is about 54 nm, according to the following relation:

$$r \approx \frac{\lambda}{2\text{NA}} = 53.74 \text{ nm}. \quad (6)$$

Figure 5 shows the observation of defects on the EUV mask by using CD-SEM and ESLI. The defect location was confirmed by CD-SEM and image reconstruction was performed on the defect site by ESLI. The bright area in the ESLI image refers to the region of high reflectivity and the dark area indicates the region of low reflectivity due to the absorber pattern or defect. A defect located on the multi-layer between absorber lines is observed in the CD-SEM image, and this corresponds to the dark point in the ESLI

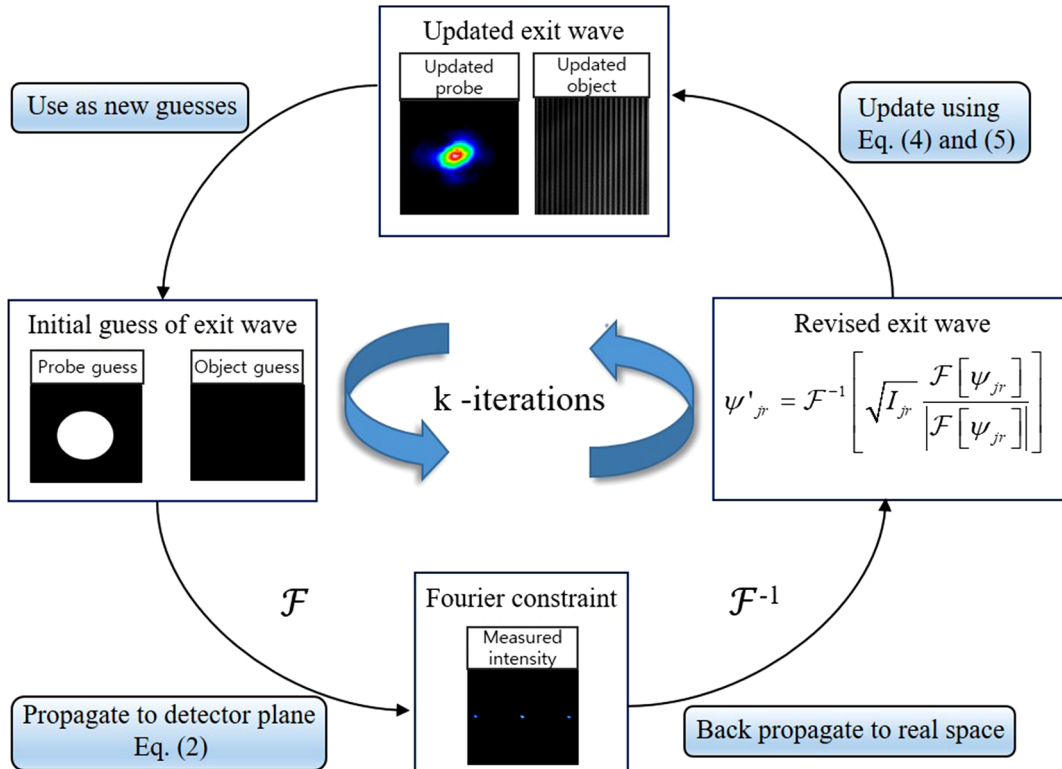


Fig. 3 Schematic process of ptychography.

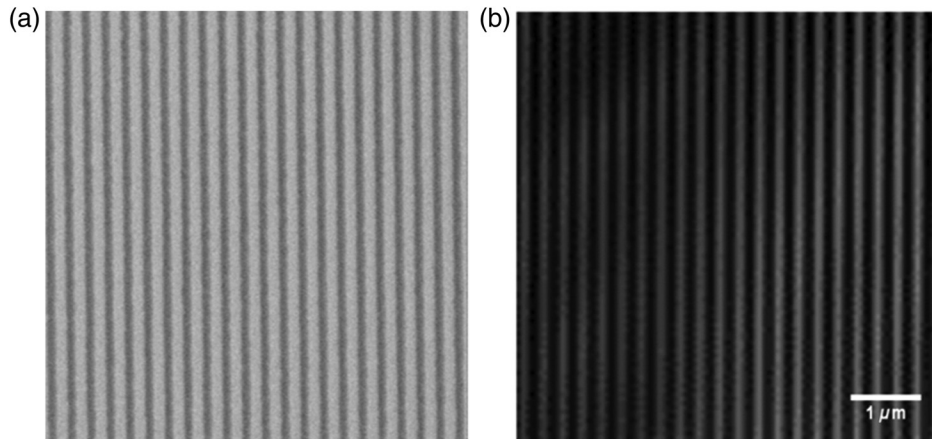


Fig. 4 Comparison of mask images (128-nm HP L/S) obtained by (a) CD-SEM and (b) ESLI.

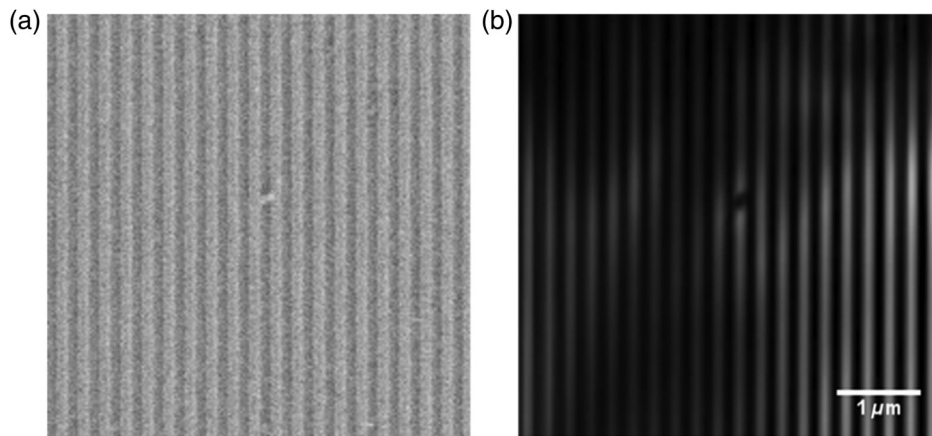


Fig. 5 Comparison of defects observed with (a) CD-SEM and (b) ESLI (128-nm HP L/S EUV mask).

image. Therefore, it can be confirmed that the ESLI system can capture the bridge-type defect on the EUV mask.

A similar image distortion may occur due to contamination on the EUV pellicle. It is generally known that particles over 10- μm size will influence the wafer pattern.^{25,26} Therefore, pellicle quality should be confirmed by checking the presence of printable defects before inserting into the EUV scanner. Although particles of micrometer scale can be easily observed even by using optical microscope (OM), their printability in EUV wavelength can be hardly confirmed by nonactinic

techniques. Therefore, accurate pellicle qualification using actinic wavelength should be performed.

We used the ESLI system to investigate the printability of particles on the pellicle surface. For this verification, a SiN_x freestanding membrane of 40-nm thickness was fabricated and intentionally contaminated by Fe particles, which are known to be one of the major contaminants during lithography process through spin-dry method.²⁶ Figure 6 shows the angular spectrum image of EUV light reflected by multilayer with SiN_x pellicle and the transmittance map measured by

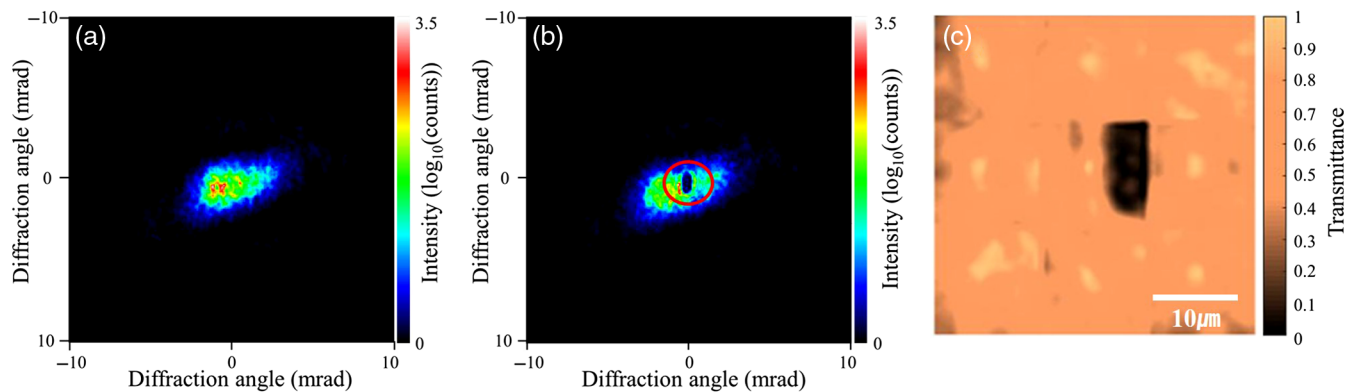


Fig. 6 Angular spectrum image: (a) before contamination and (b) after contamination (red circle implies position of contaminant). (c) Transmittance map of contaminated pellicle measured by ESLI.

ESLI. Figures 6(a) and 6(b) are angular spectrum images before and after contamination, respectively. The red circle in Fig. 6(b) indicates the loss of EUV light due to the presence of contaminants on the pellicle surface. ESLI can detect defect or contamination of pellicle by die-to-die comparison of pellicle transmittance. Figure 6(c) shows the transmittance map of pellicle measured by ESLI. Measurement of pellicle transmittance through ESLI was carried out by the following procedure.

- (1) Attach the EUV pellicle onto the EUV multilayer, which has no absorber patterns.
- (2) Irradiate the EUV source on the EUV pellicle and capture the reflected EUV intensity (I_1) using CCD.
- (3) Detach the EUV pellicle and capture the EUV intensity (I_2) at the same position of EUV multilayer.
- (4) Transmittance of pellicle can be calculated as I_1/I_2 . Since EUV light passes pellicle twice at a single exposure, $\sqrt{I_1/I_2}$ can be a single-pass transmittance.

Also, the EUV intensity was continuously monitored by checking the intensity reflected from the reference mirror inside the ESLI system in order to maintain the EUV light irradiated onto the pellicle at a constant level during the experiment.

The particle used for pellicle contamination was Fe with $\sim 1\text{-}\mu\text{m}$ diameter. Small size particles tend to agglomerate to reduce the surface energy, and there was a wide variation of contaminant size from $1\ \mu\text{m}$ to $>10\ \mu\text{m}$. Considering the minimum thickness of contaminants ($1\ \mu\text{m}$) formed by spindry method, significant transmittance loss is expected due to particle contamination on EUV pellicle. As shown in Fig. 6(c), the existence of $\sim 10\text{-}\mu\text{m}$ -size particle agglomerates can be clearly observed by transmittance mapping. For investigation of the impact of contaminant size on the patterning result, EUV mask having absorber patterns with contaminated pellicle was observed by ESLI.

Figure 7 shows the impact of contaminated pellicle attached on the 128-nm HP L/S EUV mask with 2.5-mm stand-off distance. Figure 7(a) shows ESLI image of the

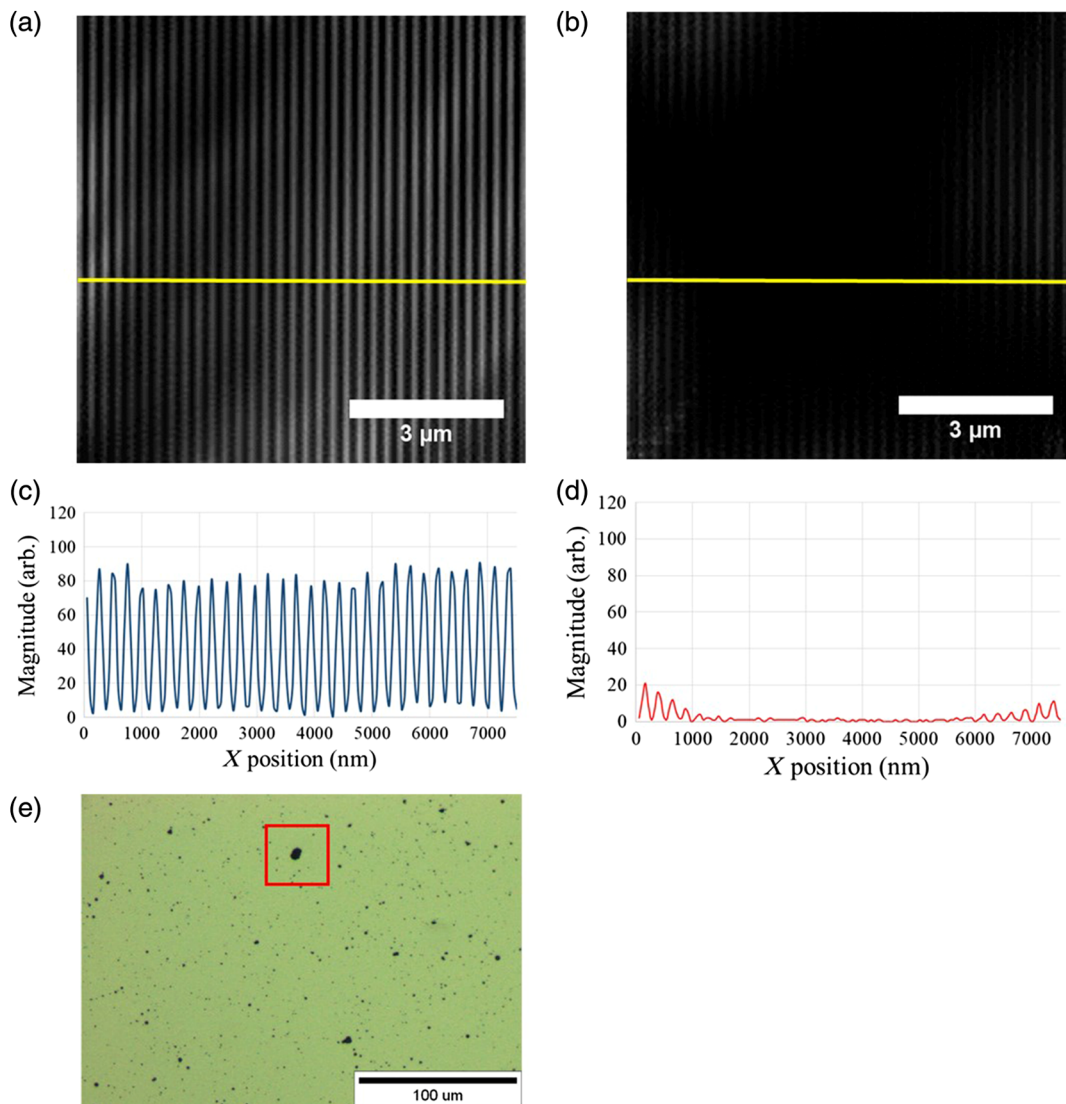


Fig. 7 Reconstructed image of EUV mask (a) without pellicle and (b) with Fe-contaminated pellicle. (c) and (d) EUV intensity profile of EUV mask image along the lines in (a) and (b), respectively, is shown. The size of Fe contaminant obtained by (d) is about $5\ \mu\text{m}$. (e) OM image of Fe-contaminated pellicle and red box represents scanned area using ESLI.

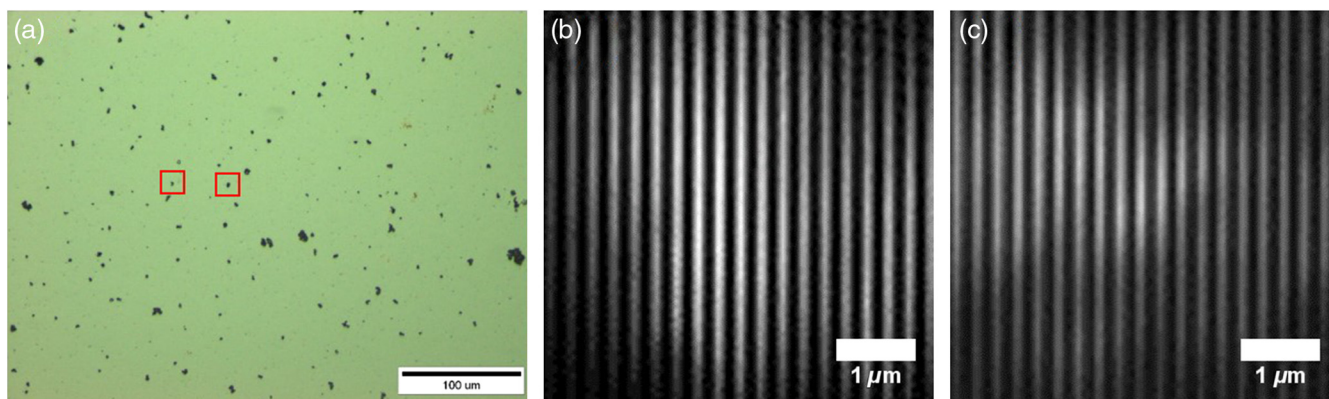


Fig. 8 (a) OM image of Fe-contaminated EUV pellicle, (b) and (c) reconstructed ESLI images of the pelliclized EUV mask with small size contaminants.

EUV mask without pellicle and Fig. 7(b) shows the mask image with Fe contaminated pellicle. As shown in Fig. 7(b), L/S image was not reconstructed in the middle of the image, where the contaminant is speculated to exist. Also, it is suspected that random scattering by the contaminant and pellicle could have resulted in blurry lines at the edge of the image.²⁷ The existence of contaminants is evident when we observe the EUV intensity profile across the L/S patterns. While the EUV intensity profile of the naked EUV mask [Fig. 7(c)] shows strong and repeated variation, L/S patterns of EUV mask with contaminated pellicle [Fig. 7(d)] do not show intensity variation due to strong absorption of EUV photons by the contaminants on the pellicle. As shown in Fig. 7(e), OM image of Fe contaminated pellicle was obtained to verify the presence of the contaminant. The size of Fe contaminant measured by OM was about 5 μm .

Contaminants on the EUV pellicle behave differently depending on their size. In general, under 10- μm -sized contaminants do not behave as fatal defects that generate yield loss. Since the EUV pellicle is located with standoff distance of 2.5 mm, 1- to 2- μm -sized contaminants are out of focus and have no effect on the final wafer pattern. This is the reason why the pellicle is used in the lithography process. Therefore, additional analysis on the influence of small size particles was performed. Figure 8 shows the OM image [Fig. 8(a)] and ESLI image [Figs. 8(b) and 8(c)] of EUV mask with pellicle contaminated by small size particles (about 1 to 2 μm measured by OM). The approximate locations of the contaminants were checked through OM and the ESLI image was scanned at that position. As shown in Fig. 7, L/S patterns through pellicles with small particles were well resolved in contrast to Fig. 7(b). Because only random contamination is available by spin-dry method and absolute positioning is not possible in current ESLI system, it is difficult to define the critical size of the contaminants on the pellicle. However, it is clear that the ESLI technique can be used to confirm the printability of contaminants on the pellicle. Although 1- to 2- μm -sized contaminants have not printed on final wafer patterns, $\sim 10\text{-}\mu\text{m}$ -sized contaminants do affect the final wafer pattern according to this result. Using ESLI, we can determine whether fatal defects exist on the pellicle in carrying out the study. The brightness variation in the ESLI image can result from random scattering by the surface of pellicle and/or frame-to-frame fluctuation of EUV intensity during ptychographic imaging.

4 Conclusions

In this study, we demonstrated ESLI, which is an actinic imaging technique, by employing HHG EUV source combined with ptychographic algorithm. The performance of the ESLI technique was evaluated by analyzing the optical property of the contaminated pellicle and EUV mask. We verified that the influence of defect on the EUV mask can be determined by the proposed technique, by comparing the ESLI results with those obtained using CD-SEM. Also, we showed the possibility of contaminant mapping of EUV pellicle by obtaining a transmittance map of contaminated pellicle. In addition, the effect of contaminant on the pellicle was investigated through printability study. Large-size ($\sim 10\ \mu\text{m}$) Fe particle agglomerates were found to contribute to wafer pattern loss. Although contaminants smaller than a certain size do not act as killing defects, they can cause random scattering, resulting in line edge roughness and blurry images. Printability study of the particles on the pellicle surface will be necessary to provide a specification for pellicle cleanliness.

Acknowledgments

This research was supported by the Ministry of Trade, Industry, & Energy (MOTIE) (Grant No. 10049007) and Korea Semiconductor Research Consortium (KSRC) support program for the development of future semiconductor devices. This research was supported by the MOTIE (Grant No. 10080526) and KSRC support program for the development of the future semiconductor device.

References

1. M. Mastenbroek, "EUV industrialization high volume manufacturing with NXE3400B," *Proc. SPIE* **10809**, 1080904 (2018).
2. J. S. Kim and J. Ahn, "Mask materials and designs for extreme ultraviolet lithography," *Electron. Mater. Lett.* **14**, 533–547 (2018).
3. K. Badger et al., "WEREWOLF: sensitivity optimization for early 7 nm EUV masks using an optical 19 \times nm inspection system," *Proc. SPIE* **10810**, 1081008 (2018).
4. K. A. Goldberg et al., "Commissioning an EUV mask microscope for lithography generations reaching 8 nm," *Proc. SPIE* **8679**, 867919 (2013).
5. D. F. Gardner et al., "Subwavelength coherent imaging of periodic samples using a 13.5 nm tabletop high-harmonic light source," *Nat. Photonics* **11**, 259–263 (2017).
6. P. Helfenstein et al., "Scanning coherent diffractive imaging methods for actinic extreme ultraviolet mask metrology," *J. Micro/Nanolithogr. MEMS MOEMS* **15**, 034006 (2016).

7. H. Stiel et al., "Soft x-ray nanoscale imaging using highly brilliant laboratory sources and new detector concepts," *Proc. SPIE* **10243**, 1024309 (2017).
8. D. Mamezaki et al., "Imaging performance improvement of coherent extreme-ultraviolet scatterometry microscope with high-harmonic-generation extreme-ultraviolet source," *Jpn. J. Appl. Phys.* **56**, 06GB01 (2017).
9. C. L. Porter et al., "General-purpose, wide field-of-view reflection imaging with a tabletop 13 nm light source," *Optica* **4**, 1552–1557 (2017).
10. J. Na et al., "Application of actinic mask review system for the preparation of HVM EUV lithography with defect free mask," *Proc. SPIE* **10145**, 101450M, (2017).
11. T. Yamane and H. Watanabe, "Application of EUV dark field image for EUVL mask fabrication," *Proc. SPIE* **10454**, 104540N (2017).
12. P. W. Wachulak et al., "A desktop extreme ultraviolet microscope based on a compact laser-plasma light source," *Appl. Phys. B* **123**, 25 (2016).
13. J. Doh et al., "Effect on critical dimension performance for carbon contamination of extreme ultraviolet mask using coherent scattering microscopy and in-situ contamination system," *Jpn. J. Appl. Phys.* **51**, 06FB04 (2012).
14. J. Doh et al., "Evaluation of lithographic performance of extreme ultraviolet mask using coherent scattering microscope," *J. Vac. Sci. Technol. B Nanotechnol. Microelectron.* **30**, 06F504 (2012).
15. S. Lee et al., "Carbon contamination of EUV mask and its effect on CD performance," *Curr. Appl. Phys.* **11**, S107–S110 (2011).
16. J. U. Lee et al., "Actinic critical dimension measurement of contaminated extreme ultraviolet mask using coherent scattering microscopy," *J. Vac. Sci. Technol. B Nanotechnol. Microelectron.* **32**, 031601 (2014).
17. D. G. Woo et al., "Coherent scattering microscopy as an effective inspection tool for analyzing performance of phase shift mask," *Opt. Express* **24**, 12055–12062 (2016).
18. D. Attwood and A. Sakdinawat, *X-rays and Extreme Ultraviolet Radiation: Principles and Applications*, Cambridge University, Cambridge (2017).
19. H. M. L. Faulkner and J. M. Rodenburg, "Movable aperture lensless transmission microscopy: a novel phase retrieval algorithm," *Phys. Rev. Lett.* **93**, 023903 (2004).
20. A. M. Maiden and J. M. Rodenburg, "An improved ptychographical phase retrieval algorithm for diffractive imaging," *Ultramicroscopy* **109**, 1256–1262 (2009).
21. M. Beckers et al., "Drift correction in ptychographic diffractive imaging," *Ultramicroscopy* **126**, 44–47 (2013).
22. M. Guizar-Sicairos and J. R. Fienup, "Phase retrieval with transverse translation diversity: a nonlinear optimization approach," *Opt. Express* **16**, 7264–7278 (2008).
23. F. Zhang et al., "Translation position determination in ptychographic coherent diffraction imaging," *Opt. Express* **21**, 13592–13606 (2013).
24. A. Maiden, D. Johnson, and P. Li, "Further improvements to the ptychographic iterative engine," *Optica* **4**, 736–745 (2017).
25. H.-K. Oh et al., "Influence of a wrinkle in terms of critical dimension variation caused by transmission nonuniformity and a particle defect on extreme ultraviolet pellicle," *J. Micro/Nanolithogr. MEMS MOEMS* **16**, 041008 (2017).
26. S. S. Kim et al., "Progress in EUV lithography toward manufacturing," *Proc. SPIE* **10143**, 1014306 (2017).
27. I. Mochi et al., "Experimental evaluation of the impact of EUV pellicles on reticle imaging," *Proc. SPIE* **10810**, 108100Y (2018).

Dong Gon Woo received his BS degree from Hanyang University in materials science and engineering. Currently, he is working as a graduate student in the division of materials science and engineering at Hanyang University. His main research is about actinic inspection technique of EUV lithography.

Jinho Ahn received his BS and MS degrees from Seoul National University in 1986 and 1988, respectively, and his PhD in materials science and engineering from the University of Texas, Austin, in 1992. He worked for the NEC Microelectronics Research Laboratory, Tsukuba, Japan (1993 to 1995), before joining Hanyang University in 1995 as a professor of materials science and engineering. He has led several national projects on advanced lithography, authored more than 160 technical papers, and invented more than 45 patents. He is a member of the National Academy of Engineering of Korea and a board member for the National Nano Infrastructure Association and National R&D Information Management Committee.

Biographies of the other authors are not available.